

A WORKFLOW FOR RAPID DESIGN, SIMULATION, FABRICATION, AND SUBSCALE FLIGHT-TESTING OF NOVEL AIRCRAFT CONCEPTS

Imon Chakraborty[1], Bikash Kunwar[1], Stefanus Putra[1], Rajan Bhandari[1] & Cole McCormick[1]

[1]Vehicle Systems, Dynamics, and Design Laboratory, Department of Aerospace Engineering, Auburn University, Auburn, AL, USA

Abstract

The Vehicle Systems, Dynamics, and Design Laboratory has developed a four-step workflow for rapid design, control law development, simulation, prototyping, and subscale flight-testing aimed at risk reduction of novel vertical takeoff and landing configurations that transition between vertical and forward modes of flight. The workflow involves the Parametric Energy-based Aircraft Configuration Evaluator conceptual sizing and optimization framework, the Modular Aircraft Dynamics and Control Algorithm Simulation Platform for flight simulation and control law development, a dual-purpose ground control station to support simulation and flight-testing, and a cost-effective manufacturing strategy utilizing additive manufacturing. The workflow is demonstrated using the example of a multi-tiltrotor configuration, the VT-03-s Shadow, which was developed and successfully flight-tested using this workflow.

Keywords: rapid prototyping, simulation, Simplified Vehicle Operations, subscale flight-testing

1. Introduction

Since 2023, the Vehicle Systems, Dynamics, and Design Laboratory (VSDDL), part of the Department of Aerospace Engineering at Auburn University, has developed and applied a four-step research and development (R&D) workflow (Fig. 1) for design optimization, control law development, flight simulation, and subscale flight-testing of novel vertical takeoff and landing (VTOL) aircraft configurations. This workflow has been successfully applied to subscale lift-plus-cruise, tilt-wing, multi-tiltrotor, and wingless multi-rotor configurations. The workflow steps are the following:

1. Sizing, performance analysis, and optimization: Using VSDDL's *Parametric Energy-based Aircraft Configuration Evaluator (PEACE)* conceptual sizing framework, the subscale aircraft is sized to meet certain payload, endurance, and point performance requirements while using commercial off-the-shelf (COTS) propulsion, energy, and avionics systems components. Op-

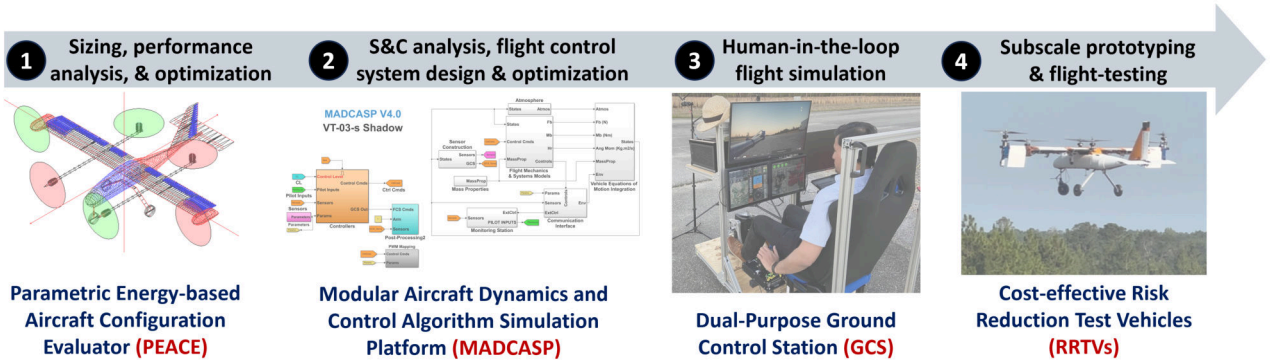


Figure 1 – VSDDL workflow for subscale aircraft design, fabrication, and flight-testing

timization, if desired, is performed by linking the PEACE framework with the Non-dominated Sorting Genetic Algorithm II (NSGA-II) optimizer. The outputs from this step include geometry definition, component-based weight build-up, center-of-gravity and inertia estimate, and identification of COTS systems components.

2. Stability and control analysis, flight control system design and optimization: This step uses *Modular Aircraft Dynamics and Control Algorithm Simulation Platform (MADCASP)*, a MATLAB & Simulink-based framework, to perform trim analysis, stability and control analysis, flight control law development, and real-time closed-loop flight simulation. The outputs are the flight control system (FCS) architecture(s) of interest and accompanying parameter sets and gain schedules.
3. Human-in-the-loop flight simulation: The interactions of the pilot with the FCS and all planned flight-test profiles are simulated using a dual-purpose Ground Control Station (GCS) running in real-time in *simulation mode* (driven by MADCASP) to verify pilot-vehicle performance, refine the FCS and planned maneuvers (if required), and de-risk the flight-test program.
4. Subscale prototyping and flight-testing: Detailed design of the vehicle using Computed Aided Design (CAD) tools follows using the outputs from conceptual design. The manufacturing strategy is aimed at fabricating cost-effective Risk Reduction Test Vehicles (RRTVs) with significant use of modular, 3-D printed structural components. The RRTVs, which can be repaired easily in the field (for minor damage) or in the laboratory (for major damage) and replaced cost-effectively (for a total loss), allow novel FCS architectures for novel VTOL platforms to be tested and refined through an accelerated and cost-effective subscale flight-test program.

The VSDDL R&D workflow is demonstrated for the VT-03-s Shadow (VT: vectored thrust, -s: subscale) multi-tiltrotor subscale aircraft shown in Fig. 2. Key characteristics of the aircraft are summarized in Table 1. It is a high-wing aircraft with a conventional tail and fixed tricycle landing gear with a castering nosewheel. Its propulsion system comprises four individually actuated tilting main propulsors (two at the wingtips, two on the front ends of the booms) and two fixed lift propulsors (aft ends of the booms), each propulsor comprising a fixed-pitch propeller directly driven by an electric motor.

At the time of writing, Shadow has been successfully transitioned between vertical and forward flight modes and operated in both VTOL and conventional takeoff and landing (CTOL) modes [1]. Transitions have been demonstrated using the Trajectory Control System (TCS), a FCS architecture aimed at Simplified Vehicle Operations (SVO), as well as the Tactical Maneuvering System (TMS), aimed at facilitating more aggressive maneuvering [2]. Maneuver sequences for system identification in the hover flight condition have also been flown and corresponding on-axis transfer functions identified [3].

The VT-03-s Shadow aircraft is based on the NASA RAVEN-SWFT subscale aircraft being flight-tested at NASA Langley Research Center [4]. The two aircraft are approximately the same size geometrically. However, Shadow uses fixed-pitch propellers while RAVEN-SWFT uses variable-pitch propellers. The two aircraft also have different FCS architectures and associated philosophy.

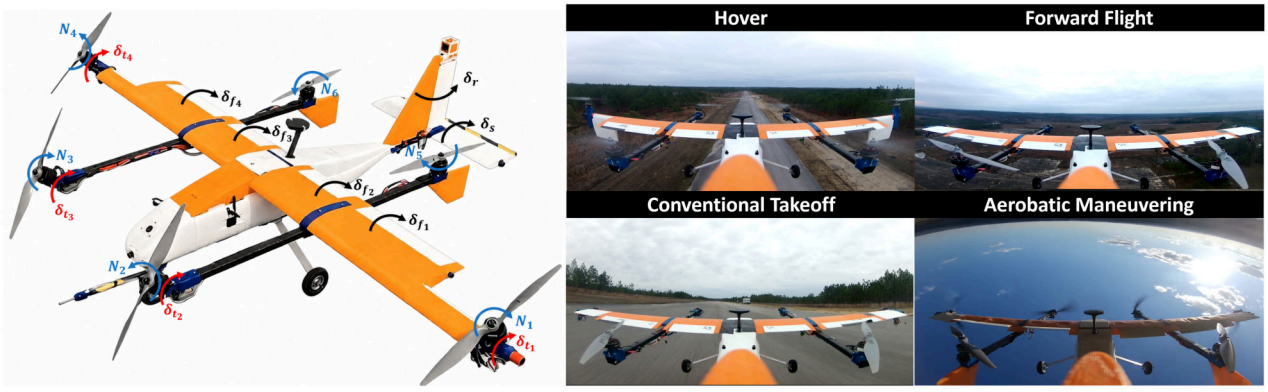


Figure 2 – VSDDL VT-03-s Shadow subscale multi-tiltrotor aircraft

Table 1 – VT-03-s Shadow - key characteristics

Propulsion	
Motors ($\times$6)	SunnySky XS X4112S KV450
Main Propeller ($\times$4)	APC 15$\times$10 E/EP fixed-pitch
Lift Propeller ($\times$2)	APC 15$\times$4 E/EP fixed-pitch
Main Battery	Hoovoo 10000 mAh 6S LiPo
Avionics Battery	HRB 3000 mAh 4S LiPo
ESC	Zubax Myxa B
Avionics & Sensors	
Flight Controller	CubePilot Cube Orange
GPS	Here3+ GPS
Airspeed Sensor	MATEKSYS ASPD-4525
LiDAR	TFmini-S
Telemetry	RFD 900X-US
FPV	Walksnail Avatar GT digital
Geometry	
Wingspan	1.7 m / 5.6 ft
Length	1.32 m / 4.32 ft (excluding pitot)
Length	1.60 m / 5.24 ft (including pitot)
Mass Properties	
Gross Weight	8.18 kg / 18.03 lb
Body-fixed axes	forward-right-down
Origin	Nacelle 1,4 pivot axis on centerline
x_{cg}, y_{cg}, z_{cg}	$\{0, 0, 6.20\}$ cm / $\{0, 0, 2.44\}$ in
Inertias I_{xx}, I_{yy}, I_{zz}	1.35, 0.82, 1.72 kg·m^2

2. VSDDL Research and Development Workflow

The four-step VSDDL workflow, shown in Fig. 1, starts with conceptual design and sizing, followed by development of control laws, real-time piloted simulation, and finally flight-testing. Each step is described with respect to the VT-03-s Shadow R&D effort.

2.1 Step 1: Vehicle sizing, performance analysis, and optimization

The aircraft is sized to a set of performance requirements using the PEACE framework, which can be wrapped within an optimization scheme to perform optimization.

2.1.1 Aero-propulsive performance model (APPM)

The APPM uses a build-up approach to compute the aero-propulsive loads on the aircraft in a computationally tractable manner. The computed loads are summed over the aircraft geometry and moments translated to the moment reference center to obtain net aero-propulsive reactions along the body axes. The same APPM is used in the PEACE and MADCASP frameworks, which allows the sized/optimized aircraft generated in Step 1 to become an input for simulation and control law development in Step 2. The APPM is linked to the aircraft geometry definition in PEACE (shown in Fig. 3) and is updated per sizing iteration.

Lifting surfaces are modeled using a strip theory-based approach, where spanwise sections are analyzed for lift, drag, and pitching moments, extended to a wide range of angles of attack using Viterna equations [5, 6]. A reduced-order model (ROM) is used to represent downwash distributions that depend on geometric and aerodynamic parameters such as aspect ratio, taper ratio, and sweep [7]. Control surfaces are analyzed in a similar manner, with adjustments for deflection and spanwise positioning, incorporating both lift and drag contributions [8]. Non-lifting components, such as the fuselage and nacelles, use lookup tables generated using FlightStream® to calculate aerodynamic loads, while landing gear drag is determined empirically.

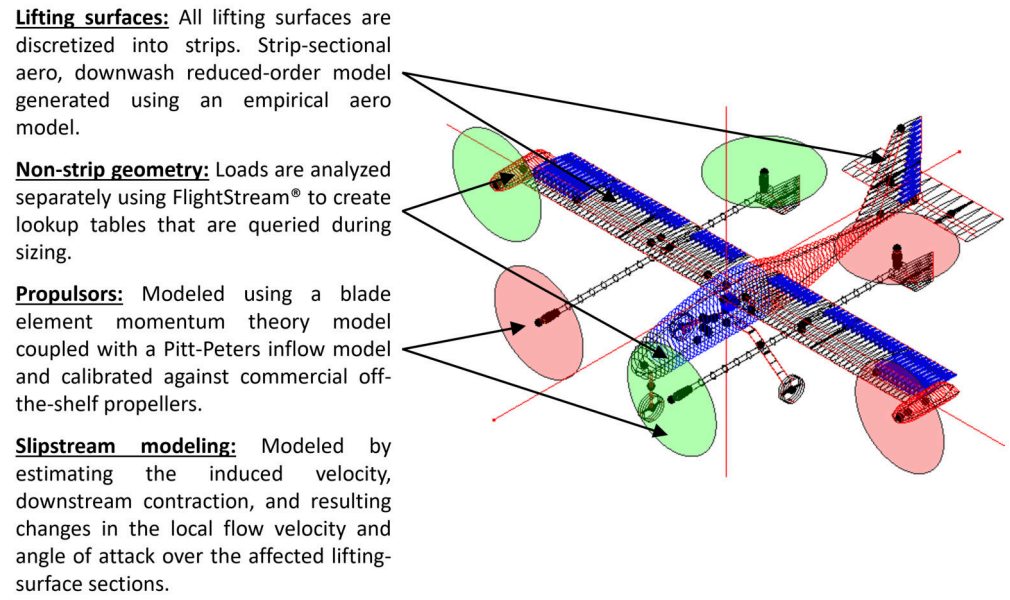


Figure 3 – Parametric geometry generated from PEACE and APPM development approach

Propulsor loads are calculated using a blade element momentum theory (BEMT) propeller model coupled to a 7-state Pitt-Peters dynamic inflow model with wake distortion effects [9]. The inflow dynamics are modeled using three states representing mean induced inflow, longitudinal inflow gradient, and lateral inflow gradient. The wake distortion is modeled using four additional states representing wake skew, spacing, longitudinal, and lateral wake curvature. The BEMT model is calibrated against manufacturer propeller performance data [10] by using a gradient-based optimizer to determine calibration factors that minimize the difference between published and predicted thrust and power at different RPMs and advance ratios.

A semi-empirical propeller slipstream model is used to determine the modification to the freestream velocity and incidence angle caused by propellers (1-4) on the strips present downstream of them. Additional details regarding the slipstream model are provided in prior work by the authors [5].

2.1.2 PEACE Framework

PEACE is a MATLAB-based sizing and optimization framework developed at VSDDL and successfully applied to novel aircraft and propulsion system architectures [11, 12, 13]. The eXtended Design Structure Matrix (xDSM) diagram in Fig. 4 shows the workflow of PEACE integrated with a genetic algorithm optimizer. Sizing starts with an initial MTOM estimate, a baseline OpenVSP geometry and specified technology states-of-the-art.

The inner convergence loop, driven to convergence by the *OEM Converger*, operates on the maximum takeoff mass (MTOM) of the current iteration (or the starting guess for the first iteration). Within it, the *Geometry Updater* updates the aircraft dimensions based on chosen design variables and specified geometry update rules. The *APPM Updater*, as the name suggests, then updates the APPM based on the revised geometry. The *S&C Sizer* sizes components such as stabilizers based on specified dynamic stability constraints. The *Power Sizer* evaluates nominal and off-nominal point performance constraints to determine the constraining scenarios that size propulsion system components. The *OEM and Mass Properties Calculator* determines the operating empty mass (OEM) based on component weight estimation relationships, center of gravity (CG) location, and an inertia tensor estimate. The *NAEM Calculator* computes the net available energy mass (NAEM) by subtracting the given payload and computed OEM from the iteration MTOM. The *OEM Converger* addresses circular dependencies among the above modules by iterating them to convergence.

The outer convergence loop, driven to convergence by the *Mass/Energy Converger* executes the *Mission Analyzer* for a time-marching analysis of the specified mission profile to obtain the required

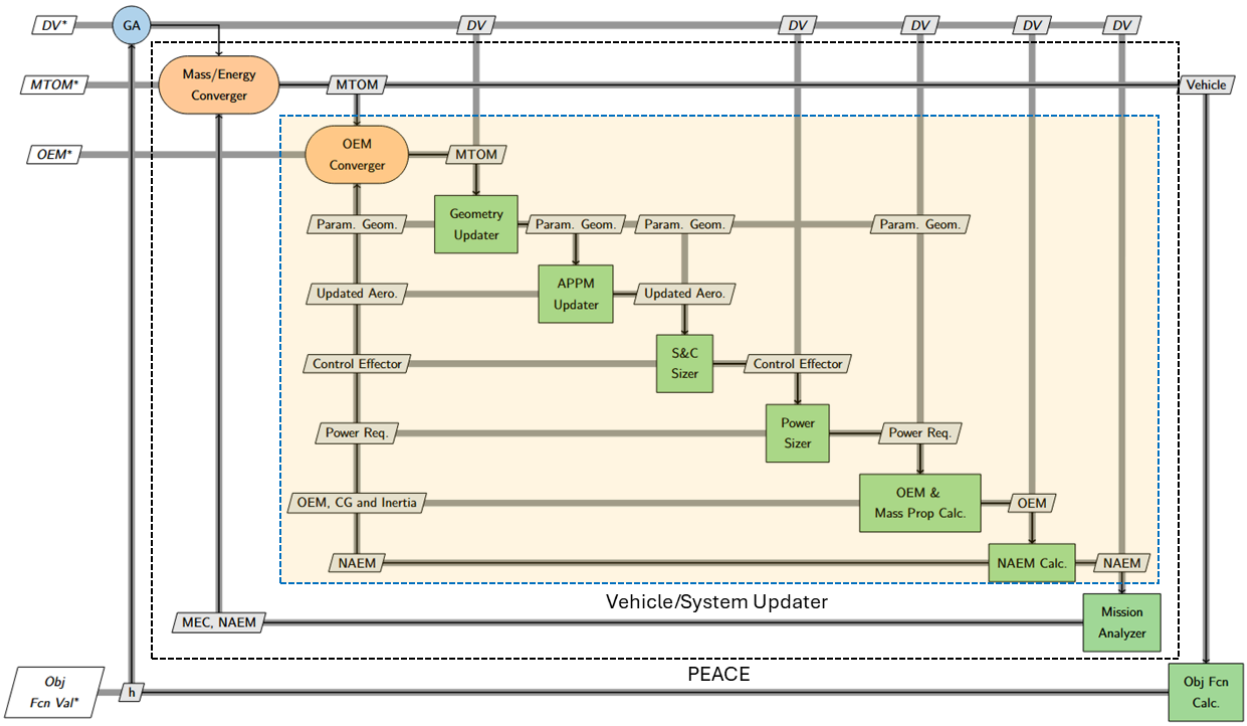


Figure 4 – XDSM representation of PEACE framework integrated with GA optimizer

propulsive energy. For sizing the aircraft based on a design mission, the MTOM is varied until the computed NAEM matches the required mission and reserve energy. For off-design missions, a mission parameter such as range or endurance is varied to obtain this energy balance.

Subscale aircraft sizing: The above workflow is modified for subscale aircraft, which make use of commercial off-the-shelf (COTS) propulsion system components such as batteries, motors, electronic speed controllers (ESCs), and propellers. Since these components must be selected from COTS options (rather than sized to exact requirements), the *Power Sizer* functions more as a *Power Analyzer* that checks whether point performance constraints are satisfied (inactive) for chosen COTS propulsion components at a given MTOM. The MTOM for a VTOL subscale aircraft is determined as the maximum weight at which a point performance constraint becomes active. With the MTOM set, the outer-loop is effectively run in off-design mode, using the *Mission Analyzer* to determine the achievable flight time (endurance) or range.

2.1.3 Sized Aircraft Characteristics

The aircraft was sized for a wing loading (WL) of 4.65 lb/ft^2 and a disc loading (DL) of 2.45 lb/ft^2. The sized aircraft has a gross mass of 8.18 kg, of which 7.07 kg is empty weight and 1.10 kg is the onboard battery. Structural mass calibration factors were computed by comparing the weights of as-built structural components with the predicted weights of the same components using the existing weight estimation relationships in PEACE for these components. The computed factors were 1.16, 1.15, and 1.34 for the fuselage, wing, and tail respectively. These computed factors were then incorporated into the weight estimation relationships to obtain agreement between predicted and as-built weights.

The resulting configuration has a wing planform area of 0.36 m^2 (3.87 ft^2) and a wingspan of 1.65 m (5.4 ft). The propulsion system consists of SunnySky XS High Power X4112S brushless motors rated at 1 kW, SunnySky X60A 2-6S brushless ESCs, APC 15$\times$4E lift propellers, and APC 15$\times$10E main propellers. The propulsive energy is supplied by a HOOVO 10,000 mAh, 6S LiPo battery.

2.2 Step 2: S&C analysis, flight control system design, and optimization

The aircraft control effectors are shown in Table 3. In hover, the nacelles (δ_{t_1}-δ_{t_4}) are oriented vertically. Rolling moments are generated through differential thrust (RPM) between propulsors (N_1, N_2, N_5) and (N_3, N_4, N_6). Pitching moments are generated using differential thrust (RPM) between propul-

Table 2 – Weight breakdown of the sized design

Component	Mass (kg)	x_{cg} (cm)	y_{cg} (cm)	z_{cg} (cm)	% MTOM
Fuselage	1.05	-4.04	0.00	8.26	12.89%
Wing	0.73	-3.15	0.00	-0.64	8.93%
Horizontal tail	0.11	-83.11	0.00	8.26	1.28%
Vertical tail	0.14	-69.77	0.00	-3.96	1.74%
Nacelles	0.28	0.89	0.00	-0.51	3.43%
Propulsor rails	0.39	-4.06	0.00	2.08	4.72%
Landing gears	0.79	5.44	0.00	23.75	9.68%
Structures	**3.49**	**-6.38**	**0.00**	**8.03**	**42.67%**
Propellers	0.27	6.96	0.00	-1.37	3.28%
Motors	1.24	3.10	0.00	-0.36	15.12%
ESCs	0.56	9.58	0.00	8.76	6.90%
Servos	0.24	-18.26	0.00	1.91	2.94%
Propulsion	**2.31**	**2.90**	**0.00**	**1.98**	**28.23%**
Avionics	0.57	3.48	-0.10	6.55	6.94%
Electrical	0.71	1.55	-0.15	3.99	8.69%
Systems	**1.28**	**2.39**	**-0.13**	**5.13**	**15.62%**
Empty weight	**7.07**	**-1.75**	**-0.03**	**5.54**	**86.52%**
Energy	**1.10**	**11.35**	**0.00**	**13.39**	**13.48%**
Gross weight	**8.18**	**0.00**	**-0.03**	**6.58**	**100.00%**
Wing planform area	0.36 m^2 (3.87 ft^2)				
Wingspan	1.70 m (5.6 ft)				
Battery	HOOVO 10,000 mAh, 6S LiPo Battery				
Motor	SunnySky XS High Power X4112S Brushless Motors, 1 kW				
ESC	SunnySky X60A 2-6S Brushless ESC				
Propeller	APC 15x4E (lift propellers), APC 15x10E (main propellers)				

sors (N_2, N_3) and (N_5, N_6). Yawing moments are generated by differential tilt of the wingtip nacelles (δ_{t_1}, δ_{t_4}), to which the outboard wing panels are keyed.

With increasing airspeed, the main propulsors tilt progressively forward and the lift propulsors gradually power down. In forward flight, the main propulsors assume a horizontal orientation ($\delta_{t_1} = \delta_{t_2} = \delta_{t_3} = \delta_{t_4} = 0$) and the lift propulsors are inactive ($N_5 = N_6 = 0$). Roll is controlled using inboard and midboard flaperons on the wing (δ_{f_1}-δ_{f_4}). Pitch is controlled using an all-moving stabilator (δ_s). The rudder (δ_r) on the vertical stabilizer is used for yaw control. When taxiing on the ground, nacelles are fully forward and differential thrust between them (N_1, N_2 versus N_3, N_4) aids in ground steering.

2.2.1 MADCASP Framework

The MADCASP framework was developed with funding from NASA Langley Research Center to facilitate stability and control analysis, flight simulation, and control law development of novel aircraft configurations. In the VSDDL R&D workflow, MADCASP is used for trim analysis, linearization of the nonlinear aircraft dynamics model for stability analysis and as a starting point for controller development, and for real-time closed-loop simulation of the aircraft and its FCS. The top-level of the Simulink model used for this purpose is shown in Fig. 5. The *Flight Mechanics and Systems Models* comprise the same APPM used by PEACE, a ground contact (landing gear) model, and second-order transfer functions for the aircraft control effectors. The *6-DOF Equations of Motion* are solved using a 4th-order Runge-Kutta scheme with a timestep of 1/60 sec (60 Hz). The FCS control laws are implemented under *Controllers* and are described subsequently. The *Atmosphere* block, in addition to modeling atmospheric properties, allows the addition of wind and turbulence to the simulation. The *Communication Interface* links the model to an external visualization of the aircraft using X-Plane

Table 3 – List of VT-03-s Shadow control effectors

#	Symbol	Description	Unit
1	δ_{f_1}	Left midboard flaperon	deg
2	δ_{f_2}	Left inboard flaperon	deg
3	δ_{f_3}	Right inboard flaperon	deg
4	δ_{f_4}	Right midboard flaperon	deg
5	δ_s	Stabilator	deg
6	δ_r	Rudder	deg
7	δ_{t_1}	Propulsor #1 nacelle angle	deg
8	δ_{t_2}	Propulsor #2 nacelle angle	deg
9	δ_{t_3}	Propulsor #3 nacelle angle	deg
10	δ_{t_4}	Propulsor #4 nacelle angle	deg
11–14	N_1–N_4	Main propulsor RPMs	RPM
15–16	N_5, N_6	Lift propulsor RPMs	RPM

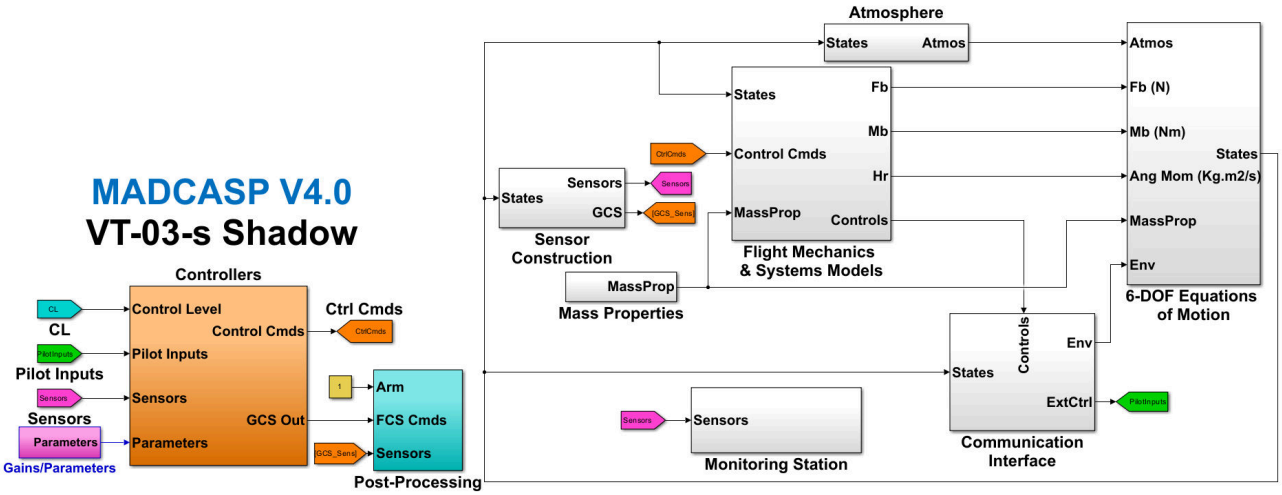


Figure 5 – Top-level of VT-03-s Shadow MADCASP Simulink model

and touchscreen instrument displays modeled using FlightGear. This setup is used in the GCS in simulation mode, and is described further subsequently.

2.2.2 Trim Analysis

In MADCASP, trim is solved as a constrained minimization problem, with the equations of motions and several other kinematic constraints modeled as equality constraints whose residuals must be driven to zero. The trim solutions over the speed envelope of the aircraft are summarized in Table 4, which shows the angle of attack (α), sideslip angle (β), normalized roll, pitch, and yaw axis control efforts (respectively $u_{lat}, u_{lon}, u_{dir}$), common nacelle angle (δ_{nac}), common main propulsor RPM (n_{mp}), common lift propulsor RPM (n_{lp}), and total power requirement (in kW). Above 30 kt airspeed, the aircraft is completely wingborne. The trim points obtained are starting points for model linearization, controller development, and gain scheduling.

2.2.3 Stability Analysis and Controller Development

Numerical linearization of the nonlinear flight dynamics model at the trim points shown in Table 4 yields linear time-invariant (LTI) systems of the form $\Delta\dot{X} = A\Delta X + B\Delta U, \Delta Y = C\Delta X + D\Delta U$. The bare airframe dynamic stability characteristics are obtained from the eigenvalues of the system matrix A, which are plotted in the real-imaginary plane in Fig. 6. In forward flight conditions (40+ kt), conventional fixed-wing modes are seen. For the longitudinal dynamics, two stable oscillatory modes, a short-period and a phugoid (long-period) oscillation, are seen. For the lateral dynamics, an oscillatory

Table 4 – Trim solutions

	Airspeed					
Parameter	0	10	20	30	40	50
α [deg]	0	0	0	0	5.90	2.05
β [deg]	0	0	0	0	0	0
u_{lat} [-1,1]	0	0	0	0	0	0
u_{lon} [-1,1]	0	0	0	0	0.30	0.16
u_{dir} [-1,1]	0	0	0	0	0	0
δ_{nac} [deg]	83	70	54	42	0	0
n_{mp} [rpm]	4380	4387	4580	5019	5249	5581
n_{lp} [rpm]	5836	5616	4906	3995	0	0
Tot. Pwr. [kW]	0.83	0.81	0.83	0.95	0.66	0.46

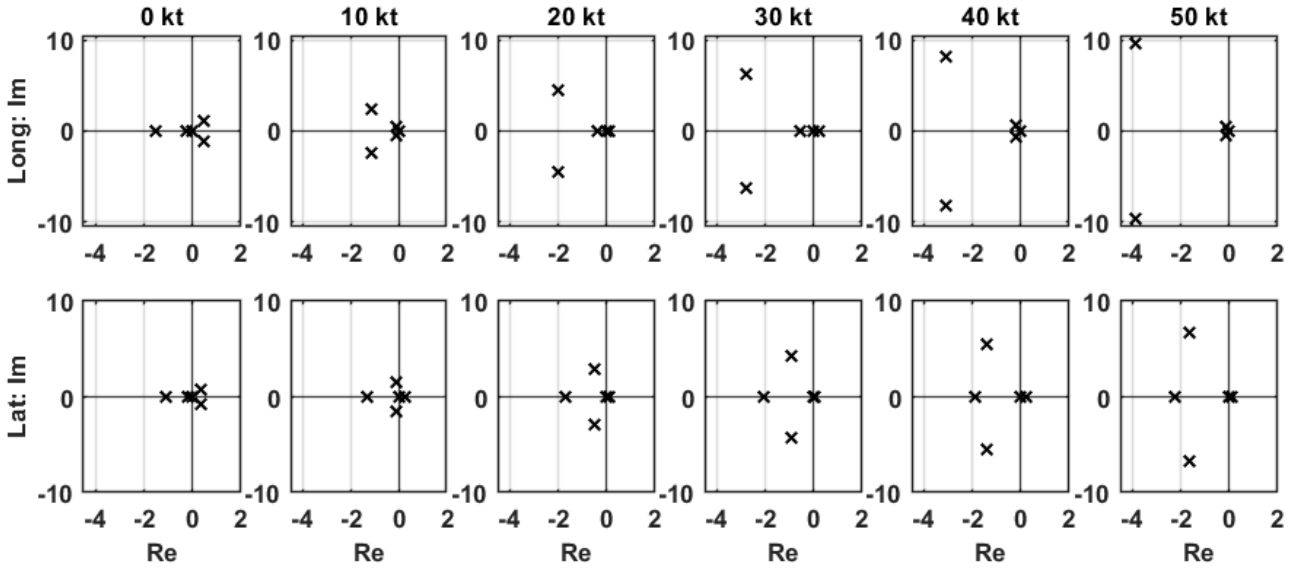


Figure 6 – Open-loop eigenvalues at selected airspeeds

Dutch roll mode, a well-damped roll mode, and a slightly divergent spiral mode are seen. At hover, there is an unstable oscillatory mode in both longitudinal and lateral dynamics common to hovering rotorcraft. The bare airframe LTI models are used as the basis for controller design. With each successive loop closure with control laws of the general form $\Delta U = -K\Delta Y = -KC\Delta X$, the stability of the closed loop system $A_{CL} = A - BKC$ is verified along with the response of the closed-loop system to step and pulse commands and several other controller performance metrics.

2.2.4 FCS Architecture

The FCS architecture at the top-level is shown in Fig. 7. The FCS can operate in one of two *operating modes*: VTOL and CTOL. The speed envelope is divided into three distinct *flight modes*: (i) *Hybrid Flight Mode (HFM)*, where aircraft weight is supported by a combination of propulsor thrust and aerodynamic lift (ii) *Transition Flight Mode (TFM)*, which represents a brief transitory mode between hybrid and forward flight modes, and (iii) *Forward Flight Mode (FFM)*, where the aircraft is wingborne with lift propulsors inactive. The FCS can operate in either TCS or TMS *control modes*.

Inceptors and response types: The pilot inceptors, shown in Fig. 8, are used to provide lateral (δ_{lat}), heave (δ_{ver}), directional (δ_{dir}), and speed (δ_{spd}) inputs to the FCS. Each is a normalized signal in the $[-1,+1]$ range. The single axis left-hand inceptor (LHI) is used to provide δ_{spd} and control airspeed and transitions between HFM, TFM, and FFM in both TCS and TMS control modes. When in TCS control mode, the LHI sets the commanded airspeed (V_{cmd}). When TMS is active, depending on the flight mode (HFM, TFM, FFM) the LHI sets the nacelle angle command and/or the main propulsor

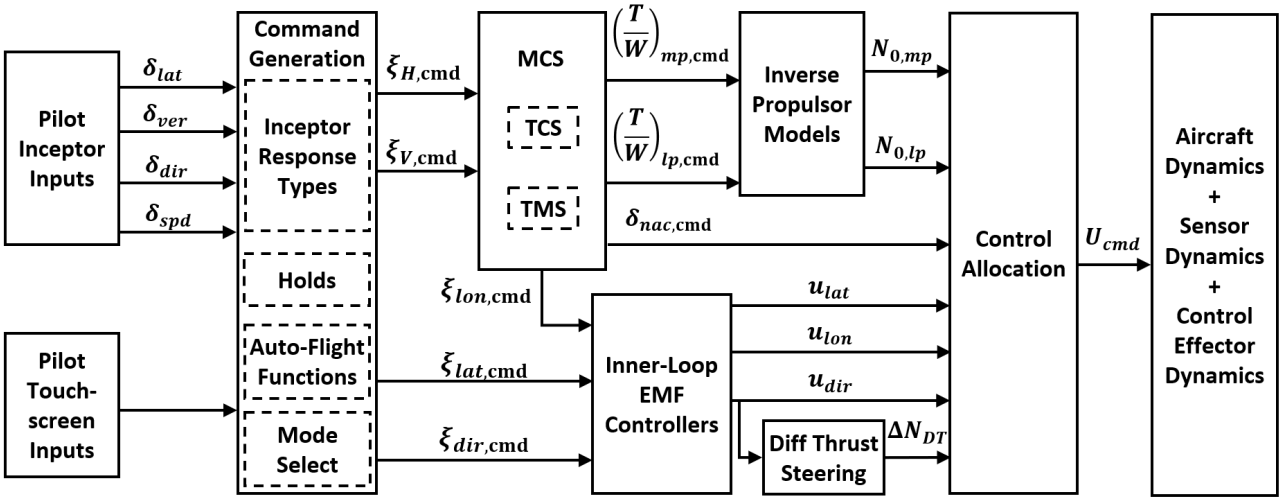


Figure 7 – VT-03-s Shadow FCS architecture

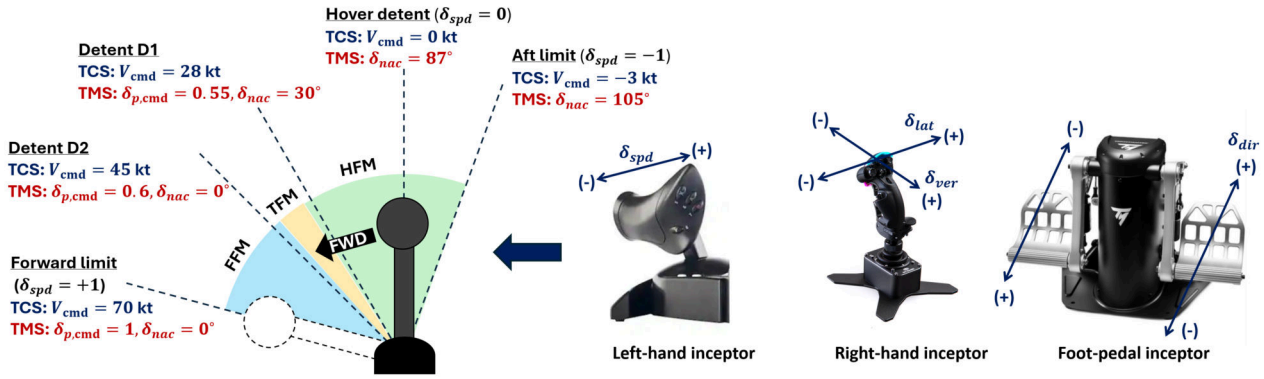


Figure 8 – VT-03-s Shadow inceptors

power setting command ($\delta_{p,\mathrm{cmd}}$). From hover, placing the LHI into detent D2 causes the vehicle to accelerate to forward flight in both TCS and TMS control modes, and from forward flight, placing the LHI in detent D1 causes the aircraft to decelerate to HFM.

Right-hand inceptor (RHI) fore/aft movements generate the δ_{ver} input, which commands vertical velocity $\dot{h}_{\mathrm{cmd}}$ in all flight modes when TCS is active. With TMS active, in HFM, δ_{ver} input generates an incremental normalized vertical thrust command $\Delta(T/W)_{\mathrm{cmd},V}$, whereas in TFM or FFM, it generates a proportional incremental normal load factor $\Delta n_{z,\mathrm{cmd}}$, which is translated into a speed-dependent pitch rate command $q_{\mathrm{cmd}} = (g/V_\infty)\Delta n_{z,\mathrm{cmd}}$.

RHI left/right movements generate the δ_{lat} input, which generates a proportionate bank angle command ϕ_{cmd} for all flight modes with TCS active. The bank command limit is 15° below 10 kt and blends to 45° at higher speeds. When the inceptor is centered ($\delta_{lat}=0$) below 10 kt, lateral velocity is automatically dissipated by an opposing bank command. Above 10 kt, lateral inputs also result

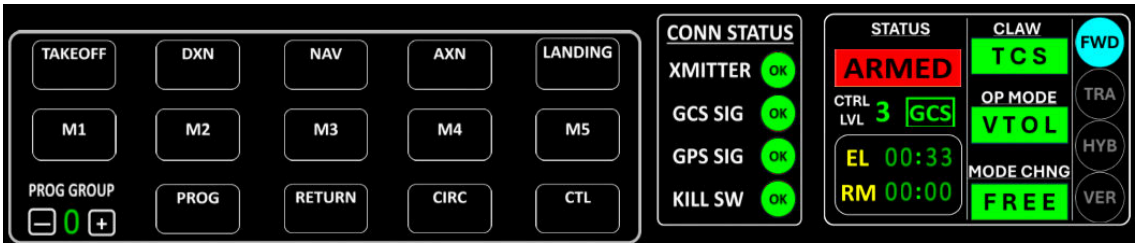


Figure 9 – Auto-flight and mode selector touchscreen panel in GCS

Table 5 – Summary of TCS and TMS holds

Hold Name	Hold Description	Command(s) Generated	Engagement Criteria	Disengagement Criteria
		TCS holds		
ALT HOLD	Altitude hold	$\dot{h}_{\text{cmd}}$	$\delta_{ver} = 0$	$\delta_{ver} \neq 0$
HDG HOLD	Heading hold	r_{cmd}	$\delta_{dir} = 0, V < 10$ kt	$\delta_{dir} \neq 0$
TRK HOLD	Track hold	$\phi_{\text{cmd}}, r_{\text{cmd}}$	$\delta_{lat} = 0, V \geq 10$ kt	$\delta_{lat} \neq 0$
POSN HOLD	Position hold	$(\dot{V}/g)_{\text{cmd}}, \phi_{\text{cmd}}$	$\delta_{lat} = 0, \delta_{spd} = 0$ $V < 3$ kt	$\delta_{lat} \neq 0 \;\|\|\; \delta_{spd} \neq 0$
		TMS holds		
BANK HOLD	Bank angle hold	p_{cmd}	$\delta_{lat} = 0, V \geq 10$ kt $\|\phi\| \leq 60^\circ, \|\theta\| \leq 30^\circ$	$\delta_{lat} \neq 0$
FPA HOLD (TFM/FFM)	Flightpath hold	q_{cmd}	$\delta_{ver} = 0, \|\phi\| \leq 60^\circ,$ $\|\theta\| \leq 30^\circ, \|\gamma\| \leq 10^\circ$	$\delta_{ver} \neq 0$

in a yaw rate command component for turn coordination, $r_{\text{cmd},tc} = (g/V_\infty)\sin(\phi_{\text{cmd}})$, and a pitch rate command component for turn compensation, $q_{\text{cmd},tc} = (g/V_\infty)\tan(\phi_{\text{cmd}})\sin(\phi_{\text{cmd}})$. When TMS is active below 10 kt, the lateral response is identical to that for TCS. At higher speeds, δ_{lat} inputs generate a proportionate roll rate command p_{cmd}. The $r_{\text{cmd},tc}$ and $q_{\text{cmd},tc}$ components are only applied when $|\phi| \leq 60^\circ$ and $|p_{\text{cmd}}| \leq 40^\circ/s$ so as not to inadvertently interfere with intended maneuvering.

The foot-pedal inceptor (FPI) generates the δ_{dir} input, which yields a proportionate yaw rate command r_{cmd} in all TCS flight modes, which is added to $r_{\text{cmd},tc}$ to yield the final yaw rate command. When TMS is active, there is a direct feed-through of the pedal input δ_{dir} in addition to the $r_{\text{cmd},tc}$ component.

Holds: The holds are pilot relief functions that allow one or more aircraft states to be maintained at their current values without requiring continuous pilot action. The holds available in TCS and TMS flight modes are summarized in Table 5, which shows the commands generated by each hold and their engagement/disengagement criteria. The pilot does not have to manually engage any hold. Holds are disengaged based on pilot inceptor input and aircraft state.

Auto-flight functions: Automatic flight (auto-flight) functions are only available in TCS control mode and can be engaged/disengaged by the pilot using the auto-flight control panel (Fig. 9). The TAKE-OFF function, whether engaged in VTOL or CTOL operating mode, generates a $\dot{h}_{\text{cmd}}$ to lift off and level off at a pre-set altitude. The CTL (centerline track) function generates steering commands to track the runway centerline by driving cross-track error to zero. The steering commands comprise coordinated bank and yaw rate commands above 10 kt in-flight, bank commands while maintaining runway heading below 10 kt in-flight, and differential thrust commands while taxiing on the ground. The CIRC (circle) function traces a constant-radius circle about a specified center while compensating for prevailing winds. The LANDING function descends at a pre-set flightpath angle (in CTOL mode) or vertical velocity (in VTOL mode), with the descent rate progressively arrested as a function of height above the ground. In CTOL mode, this automatically leads to the landing round-out and flare. The NAV (navigation) function provides lateral and vertical path guidance to track along a predefined set of mission waypoints (selected using buttons M1-M5). The NAV function can also activate TAKE-OFF, LANDING, CIRC, and CTL functions when necessary. The RETURN function brings the aircraft back to land along a specified trajectory and can be engaged by the pilot or automatically engaged if communication with the GCS is lost. PROG allows user-defined programmed maneuver sequences (mainly used for system identification) to be selected (using M1-M5) and engaged. Legacy functions DXN (departure transition) and AXN (arrival transition) respectively generate a speed command sufficient for wingborne flight or decelerate the vehicle to a hover. These functions are made redundant by the detents present in the current design of the LHI (Fig. 8).

Maneuver Control System (MCS): The MCS is a middle-loop controller which has TCS and TMS as its two control modes. For additional details regarding the control action of TCS and TMS in HFM, TFM, and FFM, the reader is referred to [2].

Table 6 – Flight mode transition logic

From → To	Criterion	TCS	TMS
HFM → TFM	$V_{\text{cmd}} > 40$ kt	✓	
	$\delta_{nac} \leq 30^\circ$	✓	✓
TFM → FFM	$V_{\text{cmd}} > 40$ kt	✓	
	$\delta_{nac} \leq 7^\circ$	✓	✓
	$\delta_{nac,\text{cmd}} \leq 1^\circ$		✓
FFM → TFM	$V_{\text{cmd}} < 30$ kt	✓	
	$V < 39$ kt	✓	
	$V < 40$ kt		✓
	$\delta_{nac,\text{cmd}} \geq 7^\circ$		✓
TFM → HFM	$V_{\text{cmd}} < 30$ kt	✓	
	$\delta_{nac} > 30^\circ$	✓	✓

Depending on the control mode active and the current flight mode, the horizontal axis command to the MCS, $\xi_{H,\text{cmd}} = \left\{(\dot{V}/g)_{\text{cmd}}, \delta_{nac,\text{cmd}}, \delta_{p,\text{cmd}}\right\}$, can comprise a normalized acceleration command $(\dot{V}/g)_{\text{cmd}}$ (TCS, all flight modes), a nacelle command $\delta_{nac,\text{cmd}}$ (TMS in HFM and TFM), or a main propulsor power setting command $\delta_{p,\text{cmd}}$ (TMS in TFM and FFM).

The vertical axis command, $\xi_{V,\text{cmd}} = \left\{\dot{h}_{\text{cmd}},\ \Delta(T/W)_{\text{cmd},V},\ q_{\text{cmd}}\right\}$, can comprise vertical velocity command $\dot{h}_{\text{cmd}}$ (TCS, all flight modes), incremental normalized vertical thrust command $\Delta(T/W)_{\text{cmd},V}$ (TMS in HFM), or pitch rate command q_{cmd} (TMS in TFM and HFM).

The outputs from the MCS are normalized thrust commands $(T/W)_{mp,\text{cmd}}$ and $(T/W)_{lp,\text{cmd}}$ for the main and lift propulsors, a nacelle angle command $\delta_{nac,\text{cmd}}$, and a longitudinal command $\xi_{lon,\text{cmd}} = \{\theta_{\text{cmd}},\ q_{\text{cmd}}\}$ comprising either a pitch attitude command θ_{cmd} or a pitch rate command q_{cmd}.

The criteria governing flight mode transitions between HFM, TFM, and FFM with TCS and TMS active are listed in Table 6. All TCS flight mode transitions involve commanded speed as a criterion. Flight mode transitions in TMS depend only on nacelle commanded and actual positions, with the exception of FFM → TFM, which also involves an airspeed threshold as a criterion.

Inner-loop controllers: The explicit model-following (EMF) inner-loop control system (Fig. 10) is implemented following [14] and generates normalized control efforts $u_{lat}, u_{lon}, u_{dir} \in [-1, +1]$ about roll, pitch, and yaw axes respectively. The two degree-of-freedom EMF control system comprises feedforward control action $u^{ff}_{(\cdot)}$ (generated through an inverse plant model) to approximately track the attitude or rate commands, and feedback control action $u^{fb}_{(\cdot)}$ (classical proportional-integral-derivative) to stabilize unstable modes, add robustness, and compensate for the approximate nature of the feedforward action. When TCS is active, the inner-loop control system tracks bank, pitch, and yaw rate commands. When TMS is active, the roll inner-loop tracks roll rate command above 10 kt, and the pitch inner-loop tracks pitch rate command in TFM and FFM. For details regarding the command model, inverse plant, and feedback action, the reader is referred to [2].

Differential thrust ground steering: Differential RPM command ΔN_{DT} between propellers N_1, N_2 and N_3, N_4, generated through feedforward and feedback control action on yaw rate command developed from pilot pedal input δ_{dir} or the CTL function, generates differential thrust to steer during taxiing on the ground in CTOL mode.

Inverse propulsor performance models (IPPMs): The required thrust is computed based on normalized thrust command and vehicle weight as $T_{\text{cmd}} = (T/W)_{\text{cmd}} \times W$. The thrust IPPMs for the APC 15X10 E/EP main propellers and APC 15X4 E/EP lift propellers compute the RPM necessary (respectively $N_{0,mp},\ N_{0,lp}$) to generate the required thrust as a function of airspeed V, estimated air

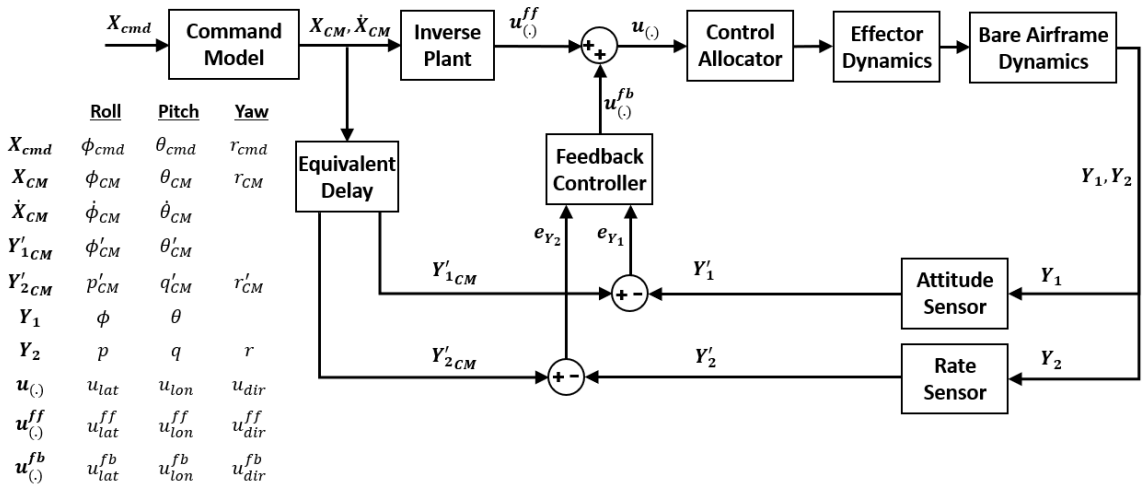


Figure 10 – Explicit model-following (EMF) inner-loop control system

density ρ, and standard sea-level air density ρ_{SL} as polynomial fits to manufacturer data (Table 7) as

$$\begin{aligned} N_{ref} &= p_1 + p_2 T_{\text{cmd}} + p_3 V + p_4 T_{\text{cmd}}^2 + p_5 T_{\text{cmd}} V + p_6 V^2 + p_7 T_{\text{cmd}}^3 + p_8 T_{\text{cmd}}^2 V + p_9 T_{\text{cmd}} V^2 + p_{10} V^3 \\ N_0 &= N_{ref} \sqrt{\frac{\rho_{SL}}{\rho}} \end{aligned} \tag{1}$$

Table 7 – IPPM coefficients for main and lift propulsors

Prop	p_1	p_2	p_3	p_4	p_5	p_6	p_7	p_8	p_9	p_{10}
MP	1358.8	281.9	46.56	-4.961	-3.370	5.068	0.0429	0.0544	-0.01978	-0.056
LP	1307.5	562.2	133.1	-21.12	-7.206	16.37	0.3762	0.3490	-0.3625	-0.338

Control allocation: The control allocation logic generates the commanded states of each of the aircraft control effectors (Table 3), yielding the control vector

$$U_{\text{cmd}}^{16\times 1} = \{\delta_{f_1}, \delta_{f_2}, \delta_{f_3}, \delta_{f_4}, \delta_s, \delta_r, \delta_{t_1}, \delta_{t_2}, \delta_{t_3}, \delta_{t_4}, N_1, N_2, N_3, N_4, N_5, N_6\}^T$$

The flaperon deflections are computed as

$$\delta_{f_1} = \delta_{f_2} = -\delta_{f_3} = -\delta_{f_4} = \Delta\delta_{f,\phi} = \Delta\delta_f^{max,\phi}\ \zeta_{\phi,f}\ u_{lat} \tag{2}$$

The stabilator and rudder deflections are computed as

$$\delta_s = -\delta_s^{max}\ u_{lon}, \qquad \delta_r = +\delta_r^{max}\ u_{dir} \tag{3}$$

The nacelle tilt angles are computed as

$$\begin{bmatrix} \delta_{t_1} \\ \delta_{t_2} \\ \delta_{t_3} \\ \delta_{t_4} \end{bmatrix} = \begin{bmatrix} 1.0 & -1.0 \\ 1.0 & 0.0 \\ 1.0 & 0.0 \\ 1.0 & +1.0 \end{bmatrix} \begin{bmatrix} \delta_{nac,\text{cmd}} \\ \Delta\delta_{nac,\psi} \end{bmatrix}, \qquad \Delta\delta_{nac,\psi} = \Delta\delta_{nac,\psi}^{max}\ \zeta_{\psi,nac}\ u_{dir} \tag{4}$$

Table 8 – Wash-in wash-out schedules (linear variations between data points)

δ_{nac}	90	80	70	60	50	40	$\leq$30
$\zeta_{\phi,mp}$	1	1	0.50	0	0	0	0
$\zeta_{\theta,mp}$	1	0.83	0.67	0.50	0.33	0.17	0
$\zeta_{\psi,mp}$	0	0	0.11	0.33	0.55	0.78	1
$\zeta_{\phi,lp}$	1	1	1	1	1	1	1
$\zeta_{\theta,lp}$	1	1	1	1	1	1	1
$\zeta_{\phi,f}$	1	1	1	1	1	1	1
$\zeta_{\psi,f}$	1	1	0.50	0	0	0	0
$\zeta_{\psi,nac}$	1	1	0.50	0	0	0	0

Main and lift propeller RPM commands are computed as

$$\begin{bmatrix} N_1 \\ N_2 \\ N_3 \\ N_4 \end{bmatrix} = \begin{bmatrix} 1.0 & +1.0 & 0.0 & +1 \\ 1.0 & +1.0 & +1.0 & +1 \\ 1.0 & -1.0 & +1.0 & -1 \\ 1.0 & -1.0 & 0.0 & -1 \end{bmatrix} \begin{bmatrix} N_{0,mp} \\ \Delta N_{\phi,mp} \\ \Delta N_{\theta,mp} \\ \Delta N_{\psi,mp} \end{bmatrix}, \qquad \begin{bmatrix} N_5 \\ N_6 \end{bmatrix} = \begin{bmatrix} 1.0 & +1.0 & -1.0 \\ 1.0 & -1.0 & -1.0 \end{bmatrix} \begin{bmatrix} N_{0,lp} \\ \Delta N_{\phi,lp} \\ \Delta N_{\theta,lp} \end{bmatrix}$$

$$\begin{aligned} \Delta N_{\phi,mp} &= \Delta N^{max}_{\phi,mp}\ \zeta_{\phi,mp}\ u_{lat} \\ \Delta N_{\theta,mp} &= \Delta N^{max}_{\theta,mp}\ \zeta_{\theta,mp}\ u_{lon} \\ \Delta N_{\psi,mp} &= \Delta N^{max}_{\psi,mp}\ \zeta_{\psi,mp}\ u_{dir} + \Delta N_{DT} \\ \Delta N_{\phi,lp} &= \Delta N^{max}_{\phi,lp}\ \zeta_{\phi,lp}\ u_{lat} \\ \Delta N_{\theta,lp} &= \Delta N^{max}_{\theta,lp}\ \zeta_{\theta,lp}\ u_{lon} \end{aligned} \tag{5}$$

The computed control surface and nacelle deflections are subject to physical deflection limits. The wash-in/wash-out parameters in Eqs. 2, 4, 5 are scheduled with respect to nacelle angle per the schedule shown in Table 8.

Step 3: Human-in-the-loop flight simulation

The subscale flight-testing campaign is de-risked by simulating flight-test profiles using a dual purpose ground control station (GCS) which can operate in simulation mode in the laboratory environment and in flight-test mode in the field with identical inceptor (Fig. 8) and display configurations. The connectivity between the GCS and the vehicle or its simulation model is shown in Fig. 11.

During flight-testing, the top screen shows a first-person view (FPV) camera feed from the aircraft. The lower touchscreens show telemetry from the vehicle. While the GCS pilot flies using the FPV feed, the remote pilot-in-command stands nearby maintaining visual line-of-sight with the aircraft and is capable of assuming control via a R/C transmitter if necessary. The flight-test engineer has duplicate displays and can update certain gains or activate system identification maneuvers in-flight. In simulation mode, the GCS is interfaced with the MADCASP flight simulation model, which drives the touchscreen displays and a rendering of the flight environment (using X-Plane Flight Simulator) on the FPV display.

The custom touchscreen displays, which are implemented using FlightGear Flight Simulator, are shown in Fig. 12. The auto-flight control panel (A) was shown previously in Fig. 9. The map display (B) shows an overlay of the waypoint grid on a North-up image of the flight-test site at Sharpe Field in Tuskegee, AL. The connection status display (C) shows connectivity between the aircraft and the GCS. The primary flight display (D) shows key aircraft states, information on holds, and vertical and lateral path deviation indicators if appropriate auto-flight modes are engaged. Above it, the arm/disarm status, flight timer, active control mode (CLAW), operational mode (OP MODE), mode change selection (FREE or LOCKED), and current flight mode (VFM, HFM, TFM, or FFM) are displayed in (E). The nacelle position indicator (F) shows the common command for the tilting nacelles ($\delta_{nac,\text{cmd}}$). The FCS display (G) shows inceptor inputs and intermediate and final FCS commands (see Fig. 7). The energy display (H) shows information on battery state and usage.

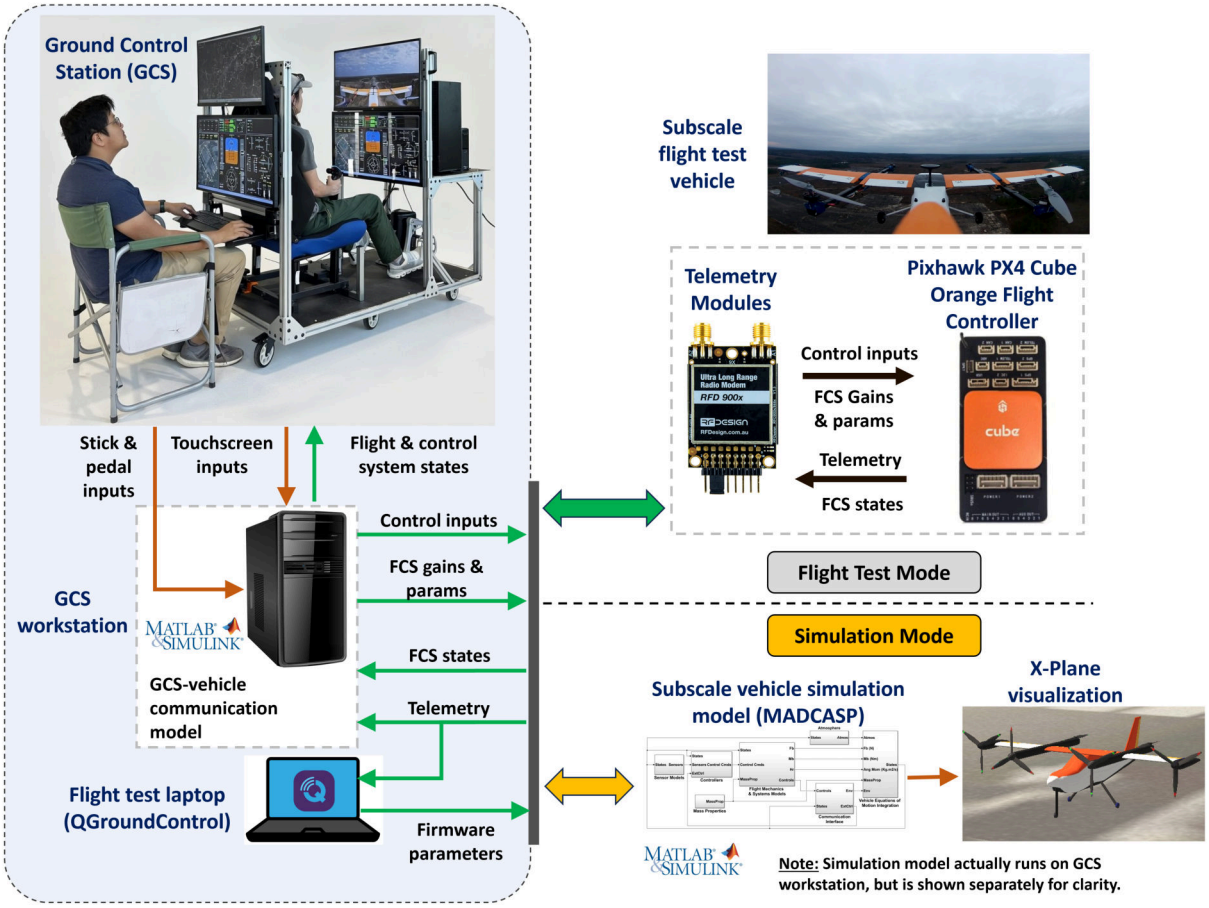


Figure 11 – GCS-vehicle and GCS-simulation connectivity

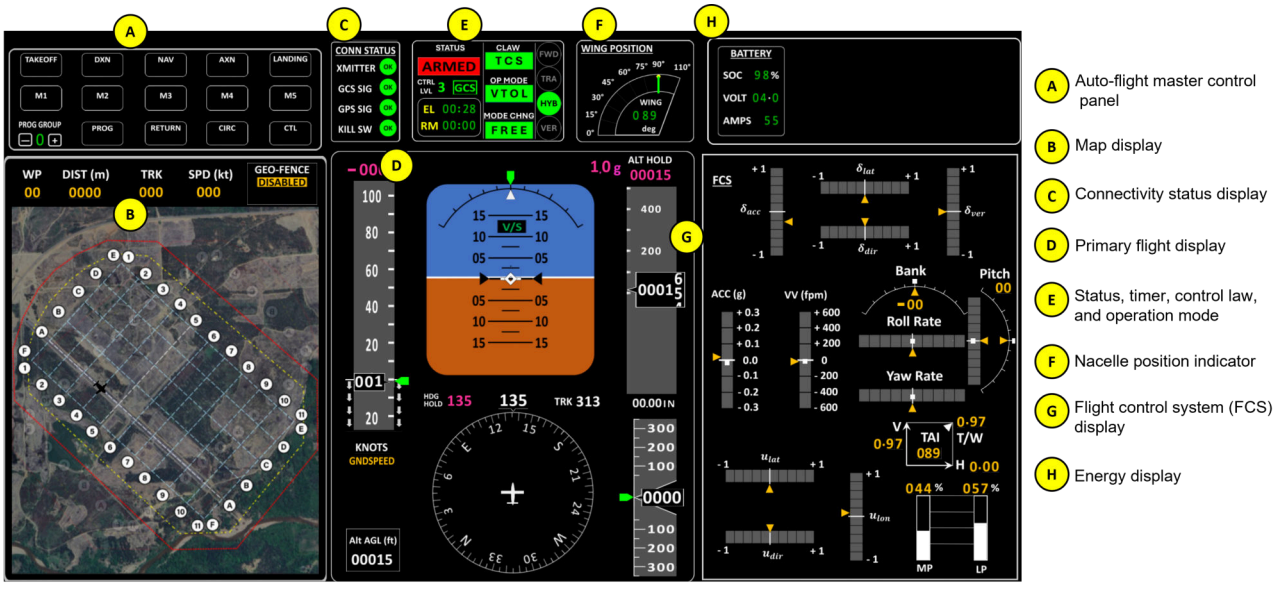


Figure 12 – GCS displays for VT-03-s Shadow

2.3 Step 4: Subscale prototyping and flight-test preparations

The prototype is fabricated using a combination of addictive manufacturing (3D printing) and off-the-shelf components, with a focus on rapid, cost-effective manufacturing and assembly. The steps involved are detailed design, fabrication and assembly, measurement of mass properties of the as-built vehicle, propulsor characterization, deployment of control laws, power-up and systems checks.

2.3.1 Detailed design

Detailed design is performed through computer-aided design (CAD) using SolidWorks based on the converged design output from PEACE. Fuselage lines, airfoil coordinates, and other geometric parameters defined by PEACE in the conceptual design stage are directly extracted from the PEACE output. A dimensioned drawing of the final design is shown in Fig. 13. Structural layouts, avionics mountings, other miscellaneous components, and fasteners, which are not defined within the PEACE conceptual design model, are designed on a vehicle-specific basis. For VT-03-s Shadow, the structure consists of COTS carbon fiber rods with 3D-printed ribs and bulkheads forming the structural frame. The landing gear is made by bending an off-the-shelf aluminum bar into shape with COTS wheels. Aerodynamic surfaces are printed using lightweight polylactic acid (LW-PLA), with the structural 3D-printed ribs and bulkheads printed using polylactic acid plus (PLA+). The front nacelles are actuated using linear servos, while the outboard nacelles are actuated using rotary servos.

A bill-of-materials (BOM) is created based on the final detailed design and the selected off-the-shelf components. A cost breakdown by major group based on the BOM is shown in Fig. 14. Propulsion system components are the biggest contributor (40.20%), followed by avionics (37.11%) and structures (20.14%). The total cost of the latest airframe is USD 5,890 (June 2026), which, despite recent inflation and tariffs, still represents a cost-effective solution for exploratory subscale flight-testing.

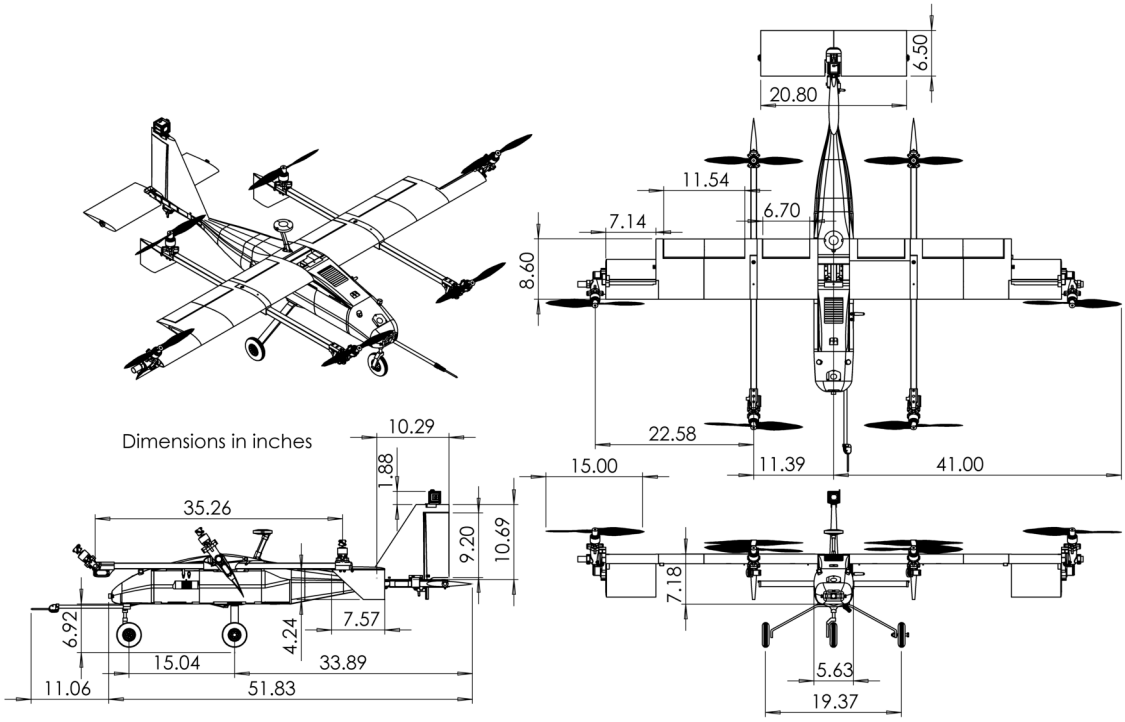


Figure 13 – VT-03-s Shadow dimensioned drawing

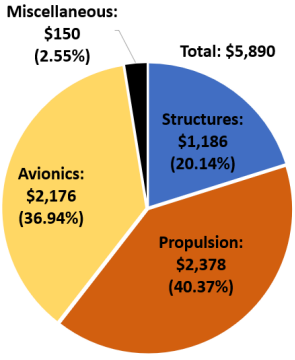


Figure 14 – VT-03-s Shadow cost breakdown

2.3.2 Fabrication and assembly

Fabrication consists of additive manufacturing using multiple VSDDL 3D-printers and a dedicated on-campus additive manufacturing shop. Machining of metal components and other carbon fiber components is done in the lab using basic machining tools or through a dedicated on-campus machine shop. Fabrication of power and avionics wiring is done in the laboratory using a soldering station and COTS connectors. The complete 3D-printing time is estimated to be 42 hours, assuming constant operation of six printers with almost no downtime.

The estimated assembly time is around 7.0 hours with two people involved. This estimate assumes that all components are fully fabricated, including the wiring. The fabrication and assembly timeline is shown in Fig. 15. It has been demonstrated that a brand new VT-03-s Shadow airframe can be fabricated, assembled, and readied for flight-testing in 49 hours with a crew of 2 people when fabrication and assembly are done simultaneously.

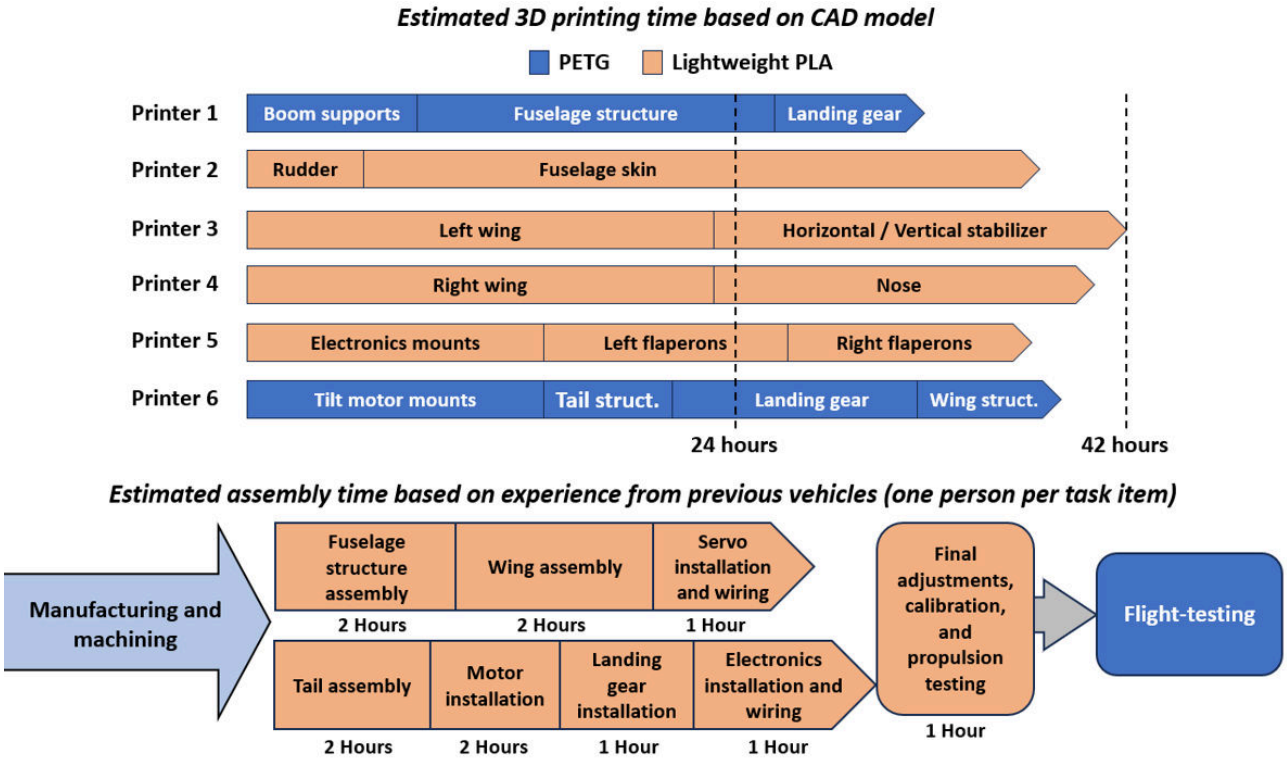


Figure 15 – VT-03-s Shadow fabrication and assembly time

2.3.3 Mass properties measurement

After the vehicle is built, the weight of the as-built vehicle is measured using weighing scales. Each of the three landing gears is placed on a weighing scale on level ground. The measured reaction forces and the landing gear wheel location are used to determine the center of gravity location using conditions of static equilibrium [15]. The moments of inertia of the as-built vehicle along the body axes and about the vehicle reference point are experimentally determined using the setup shown in Fig. 16. The swinging gear design is adopted from [16, 17] for full-scale aircraft and modified for subscale application [18]. The roll and pitch axis setups are based on the compound pendulum principle, and the yaw axis setup is based on the bifilar torsional pendulum principle. An inertial measurement unit is attached to the cradle to record and transmit attitude and angular rate measurements, which are used to determine the oscillation period by averaging the total time required to complete a number of small-amplitude oscillations. The moments of inertia are then computed from the measured time periods and rig geometry per [16].

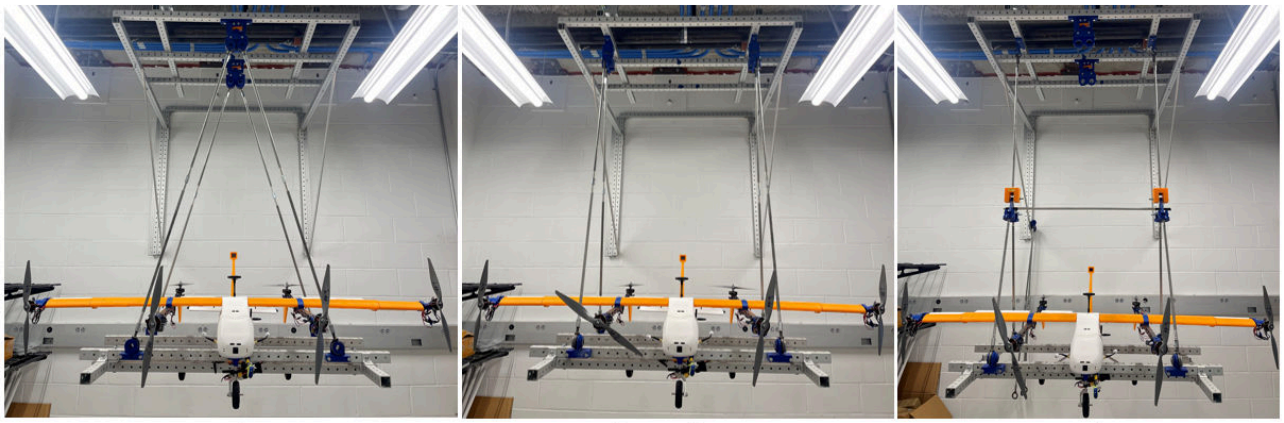


Figure 16 – Experimental setup for measurement of moments of inertia of the as-built vehicle

2.3.4 Propulsor characterization

A thrust test setup using the TYTO ROBOTICS series 1585 thrust stand (shown in Fig. 17) is used to characterize the combination of electronic speed controller (ESC), motor, and propeller used in the vehicle. Thrust, torque, and rotational speed are measured over a range of throttle settings under static conditions. The resulting throttle-to-RPM relationship is used in the feedforward model for flight testing, enabling the control system to translate RPM commands into throttle commands for the ESCs. Step-response data collected during testing are used to identify the combined ESC-motor-propeller dynamics for incorporation into the MADCASP simulation model. For both main and lift propellers for VT-03-s Shadow, which are driven by the same motor and ESC combination, the combined dynamics were seen to be adequately represented as an underdamped second-order system with undamped natural frequency $\omega_n = 20$ rad/s and a damping ratio $\zeta = 0.7$.



Figure 17 – Thrust test stand setup for motor and propeller testing

2.3.5 MATLAB/Simulink to PX4 Workflow

The control system, sensor interface, and data transmission blocks from MADCASP are deployed to the Cube Orange CubePilot using the UAV Toolbox Support Package for PX4® Autopilots in MATLAB/Simulink. The parameters and gains intended to be tunable between flights without re-building or re-flashing the code are written as PX4 parameters during code generation. These parameters are generated using an automated spreadsheet-to-YAML generator, where simulation values are used as the default entries. After deployment, the parameters can be modified through QGroundControl®. Custom messages are also implemented to send telemetry from the GCS to the vehicle, including

pilot stick inputs, touch commands, and selected tunable parameters or gains. In addition, custom messages are also used to log control system states and other variables not available through the default messages. These messages also support the transmission of vehicle telemetry to the GCS for real-time display and post-flight analysis.

3. Flight-Testing Results

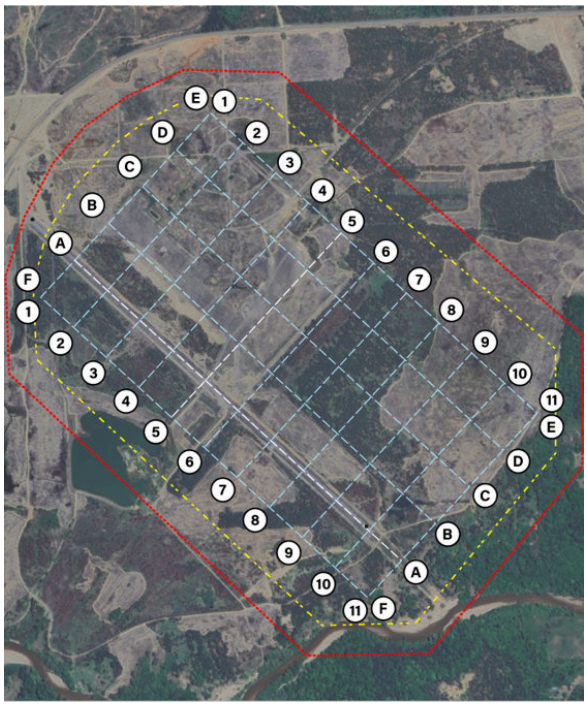


Figure 18 – Sharpe Field (AL73) in Tuskegee, AL, USA

Flight-testing of VT-03-s Shadow is conducted at Sharpe Field in Tuskegee, AL, USA at a disused airfield once used by the Tuskegee Airmen for flight-training during World War Two. The test site, shown in Fig. 18, has a 1-mile long runway (along waypoints A1-A11) that is ideal for testing transitions between hover and forward flight modes and adequate space to the north-east of the runway for sustained forward flight (in a rectangular pattern) and maneuvering.

Publicly released flight-test data (continuously updated) are summarized in Table 9. For released flight-tests, an Excel spreadsheet containing logged flight-test data along with a YouTube video containing onboard footage, external footage, and telemetry are provided. An aircraft description document (PDF) and a flight dynamics package (.zip) containing trim points, linearized models, and the nonlinear APPM of the aircraft (MATLAB .p-code) are also available.

Table 9 – Summary of VT-03-s Shadow flight-test content

#	Description	Link
1	Flight data downloads on VSDDL website	`https://vsddl.com/downloads`
2	Explanation of downloadable Shadow data	`https://youtu.be/GMnel3XPpDU`
3	Transitions using TCS	`https://youtu.be/pJQGNfNYP44`
4	Transitions using TMS, TCS-TMS in-flight	`https://youtu.be/Cu0ppG4ZjM4`
5	Roll axis system identification at hover	`https://youtu.be/LwMyi-G9sYs`
6	Pitch axis system identification at hover	`https://youtu.be/ib5GZfsmmVA`
7	Yaw axis system identification at hover	`https://youtu.be/gGvrQoxdYz0`
8	Heave axis system identification at hover	`https://youtu.be/TvqZb0YHpPE`
9	TMS transitions and aileron rolls	`https://youtu.be/8_-gitWW87I`
10	Conventional takeoff, vertical landing	`https://youtu.be/beqMvh5Dw3g`

3.1 Transitions using Trajectory Control System (TCS)

Transitions between hover and forward flight using TCS are shown in Fig. 19(a) and Fig. 19(b). Data from this flight-test was also discussed in [2] and is downloadable (see Table 9).

3.1.1 Accelerating TCS Transition (HFM→TFM→FFM)

An accelerating HFM→TFM→FFM transition from hover at 100 ft altitude to forward flight at 45 kt airspeed while tracking the runway centerline is shown in Fig. 19(a). As the aircraft accelerated in HFM, the nacelles tilted forward at an average rate of approximately $4^\circ/s$ while the pitch attitude remained level. The vertical thrust command $(T/W)_{\text{cmd},V}$ (labeled TWV) decreased as the wings generated progressively more lift, while the horizontal thrust command $(T/W)_{\text{cmd},H}$ (labeled TWH) increased to offset progressively greater drag. The altitude deviation remained minimal (≈10 ft).

At $t = 15.5$ sec, the aircraft shifted into TFM as the HFM→TFM criteria (Table 6) for TCS were met. The lift propulsors then gradually powered down while nose-up pitch command was generated to compensate for the reduction in lift propulsor thrust with an increase in aerodynamic lift. The compensation was not perfect, however, and an altitude excursion of +15 ft was encountered. At $t = 22$ sec, the aircraft shifted into FFM as the TFM→FFM criteria (Table 6) for TCS were met.

During acceleration, the NAV algorithm generated coordinated bank and yaw rate commands to track the runway centerline. The worst cross-track error (CTE) of 4.57 m (20 ft) occurred around 10 kt during the lateral mode blend. After the aircraft returned to centerline at $t = 10$ sec, the CTE remained within ±1.70 m (±5.57 ft).

Attitude control efforts $u_{lat}, u_{lon}, u_{dir}$ remained relatively low. Gradual nose-down pitch control effort $u_{lon} < 0$ developed up to around 20 kt airspeed, followed by progressive nose-up pitch control effort $u_{lon} > 0$ as the aircraft accelerated into FFM. The airspeed overshoot upon reaching FFM and the tracking of vertical velocity during TFM were deficiencies that warranted further improvement through refinement of TCS gains.

3.1.2 Decelerating TCS Transition (FFM→TFM→HFM)

A decelerating FFM→TFM→HFM transition using TCS is shown in Fig. 19(b), with a target altitude of 180 ft. At $t = 2$ sec, with the aircraft in FFM at 35 kt airspeed, the speed command was reduced to 28 kt, immediately satisfying the FFM→TFM criteria (Table 6), and resulting in the aircraft shifting into TFM. In TFM, the nacelles moved towards the vertical at approximately $+3.4^\circ/s$ while lift propellers activated and powered up progressively. Vertical flightpath was controlled using pitch attitude.

At $t = 11.1$ sec, the nacelles reached 30° angle, satisfying the TFM→HFM criteria (Table 6), resulting in a shift into HFM. Pitch attitude gradually dissipated to zero (level deck), while vertical flightpath was controlled using vertical thrust component $(T/W)_{\text{cmd},V}$, shared proportionately between main and lift propulsors. By the end of the interval shown in Fig. 19(b), the aircraft slowed to 28 kt, with nacelles at 48° angle, main propulsors at 35% power, and lift propulsors at 18% power.

While decelerating, the NAV algorithm intercepted the runway centerline coming out of a left base-to-final turn. The centerline intercept was complete by the TFM→HFM shift. Thereafter, CTE remained within ±1.33 m (±4.36 ft). No airspeed undershoot occurred during deceleration. However, the tracking of vertical velocity command during deceleration through TFM warranted further improvement.

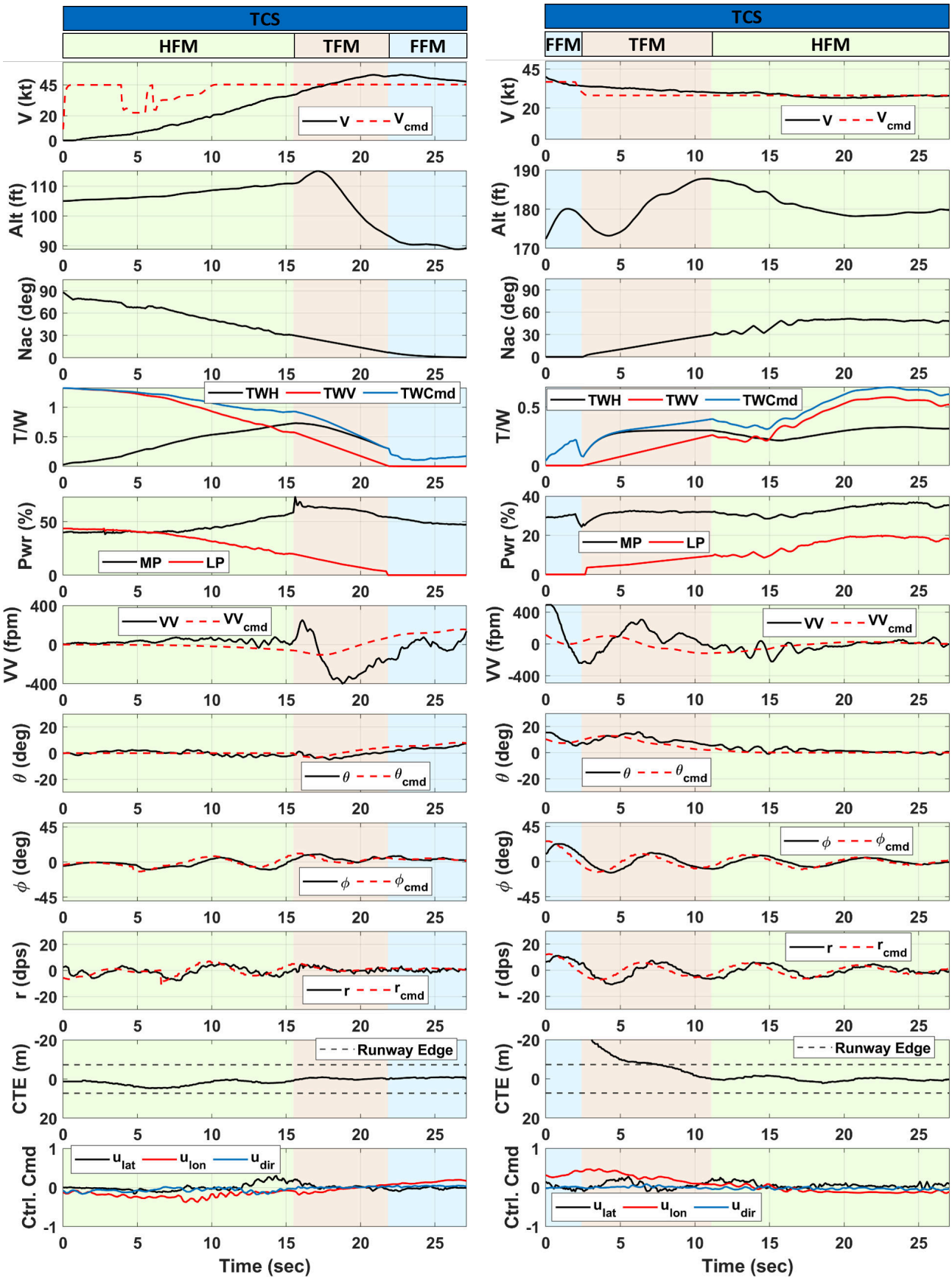
3.2 Transitions using Tactical Maneuvering System (TMS)

Transitions between hover and forward flight using TMS are shown in Fig. 20(a) and Fig. 20(b). Data from this flight-test was also discussed in [2] and is downloadable (see Table 9).

3.2.1 Accelerating TMS Transition (HFM→TFM→FFM)

To reduce risk, takeoff and vertical climb to 100 ft altitude were performed using TCS. The control mode was then switched to TMS using the touchscreen (Fig. 9). This deactivated the TCS-specific ALT HOLD, HDG hold, and POSN HOLD functions. The control mode change was transient-free.

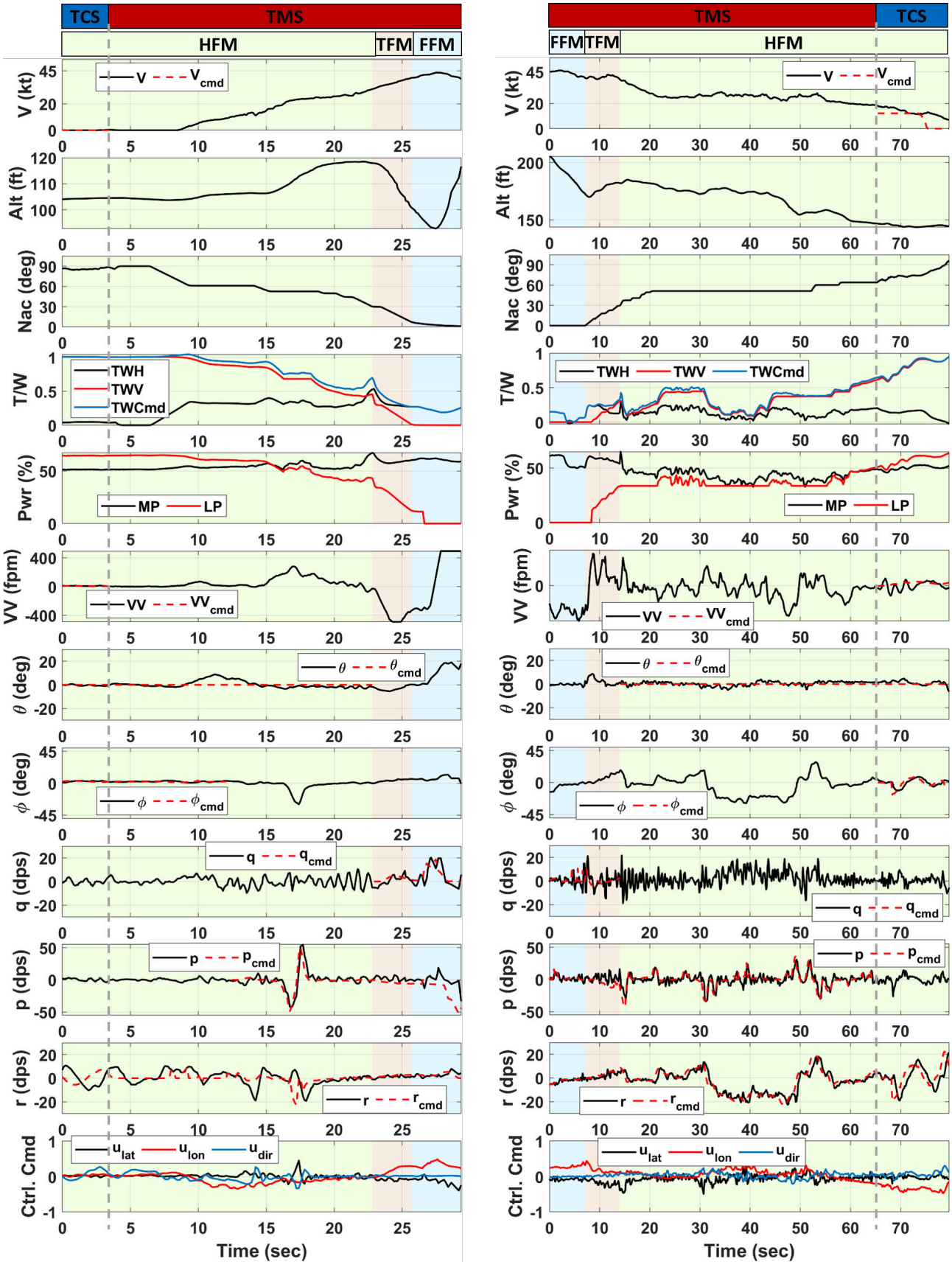
The pilot started to accelerate by using the LHI to command forward rotation of the nacelles from 90° to 60°. The nacelle movement occurred at the $15^\circ/s$ rate limit and the aircraft accelerated to



(a) Accelerating transition

(b) Decelerating transition

Figure 19 – Transitions using Trajectory Control System (TCS)



(a) Accelerating transition

(b) Decelerating transition

Figure 20 – Transitions using Tactical Manuevering System (TMS)

approximately 13 kt. At $t = 14.2$ sec, the pilot commanded 52° nacelle angle, causing the aircraft to accelerate to 24 kt. Between $t = 20$ sec and $t = 26$ sec, the pilot progressively commanded the nacelles to forward flight position at an average rate of $7^\circ/s$. The aircraft entered TFM at $t = 22.8$ sec and FFM at $t = 25.68$ sec as the corresponding mode shift criteria (Table 6) were successively met.

This flight being the first transition attempt with TMS, the pilot moved the nacelles gradually and not aggressively (at their maximum permitted rate). Even so, the acceleration to forward flight with TMS took only 17.2 sec, compared to 21.8 sec with TCS (Fig. 19(a)). A maximum performance TMS acceleration is possible in an even shorter time interval.

The pilot, accustomed to commanding bank angle using TCS, over-corrected at $t = 16$ sec while attempting to track the runway centerline as the roll response type had changed from bank command (ϕ_{cmd}) to roll rate command (p_{cmd}) once the aircraft had accelerated beyond 10 kt airspeed. This resulted in a brief -22° bank angle excursion with $\pm 50^\circ/s$ commanded roll rates and warrants further review and refinement of the $\phi_{\text{cmd}}/p_{\text{cmd}}$ lateral response blend under TMS control mode.

3.2.2 Decelerating TMS Transition (FFM→TFM→HFM)

A decelerating FFM→TFM→HFM transition performed using TMS is shown in Fig. 20(b). The pilot initiated the deceleration after completing a base-to-final turn to align with the runway by placing the LHI between detents D1 and D2 and commanding $\delta_{nac,\text{cmd}} > 7^\circ$ nacelle angle.

The FFM→TFM criteria (Table 6) were satisfied once airspeed fell below 40 kt. This activated the lift propellers, which steadily powered up thereafter. The pilot progressively commanded the nacelles to 51°. The aircraft shifted from TFM to HFM once the nacelle angle exceeded 30° (Table 6).

The pilot performed a teardrop-shaped turn (first to the right, then to the left) to reverse the direction of flight while initiating a descent. These coordinated turns occurred using roll rate command (p_{cmd}) and bank angle hold with the nacelles set to 51°.

As this was the first flight to attempt transitions using TMS, to reduce risk, the pilot switched from TMS to TCS once over the runway. Once again, the control mode change occurred predictably without any transients. The pilot landed on the runway centerline by engaging auto-flight functions CTL and LANDING.

4. Conclusions

This paper demonstrated the four-step research and development workflow developed at VSDDL to enable sizing, control law development, human-in-the-loop simulation, and subscale flight-testing of novel aircraft concepts, in particular vertical takeoff and landing designs. Since 2023, this has allowed VSDDL to successfully flight-test and transition lift-plus-cruise, tiltwing, and multi-tiltrotor concepts.

Aircraft sizing is conducted using the PEACE framework, with suitable modifications to accommodate subscale aircraft that use commercial off-the-shelf propulsion system components. The sized aircraft then flow into the MADCASP framework for stability and control analysis and control law development and optimization. A dual-purpose GCS is used for human-in-the-loop flight simulation to de-risk the flight-test program through the simulation, verification, and refinement of control laws and planned maneuver sequences prior to supporting flight-testing in the field. The manufacturing strategy, which makes extensive use of 3D printing, allows for rapidly producible, easily repairable, cost-effective subscale prototypes that are ideal for exploratory flight-testing of novel configurations and their associated novel flight control laws.

The workflow was demonstrated for the VT-03-s Shadow multi-tiltrotor configuration. Ongoing flight-testing has successfully demonstrated stable transitions between hover and forward flight mode using both the Trajectory Control System (TCS) and Tactical Maneuvering System (TMS) control modes, in addition to various autonomous flight functions including autonomous takeoff-to-landing flight with waypoint navigation. Flight-tests for system identification at hover have been conducted (and are the subject of a companion paper), with hybrid and forward flight system identification to follow.

5. Contact Author Email Address

Prof. Imon Chakraborty, email: imon@auburn.edu

6. Copyright Statement

The authors confirm that they, and/or their company or organization, hold copyright on all of the original material included in this paper. The authors also confirm that they have obtained permission, from the copyright holder of any third party material included in this paper, to publish it as part of their paper. The authors confirm that they give permission, or have obtained permission from the copyright holder of this paper, for the publication and distribution of this paper as part of the ICAS proceedings or as individual off-prints from the proceedings.

References

[1] I. Chakraborty, B. Kunwar, S.H. Putra, R. Bhandari, and H.C. McCormick. Flight-Testing of the VT-03-s Shadow Multi-Tilt-Rotor Configuration in VTOL and CTOL Operations. In *AIAA SCITECH 2026 Forum*. AIAA-2026-2084, January 2026.

[2] I. Chakraborty, B. Kunwar, S.H. Putra, R. Bhandari, and H.C. McCormick. Flight Testing of the VT-03-s Shadow Multi-Tilt-Rotor Configuration with a Maneuver Control System Enabling Simplified Vehicle Operations and Tactical Maneuvering. In *Vertical Flight Society (VFS) Forum 82*. Paper 229, May 2026.

[3] B. Kunwar, S.H. Putra, R. Bhandari, H.C. McCormick, and I. Chakraborty. Simulation Model Calibration using System Identification for a Vectored-Thrust Multi-Tilt-Rotor Configuration. In *35th Congress of the International Council of the Aeronautical Sciences (ICAS 2026)*. Paper 929, September 2026.

[4] German et al. Overview of the Research Aircraft for eVTOL Enabling techNologies (RAVEN) Activity. In *AIAA AVIATION 2023 Forum*, San Diego, CA, June 2023. AIAA-2023-3924.

[5] Imon Chakraborty and Aashutosh Aman Mishra. Sizing of Tilt-Wing Aircraft with All-Electric and Hybrid-Electric Propulsion. *Journal of Aircraft*, 60(1):245–264, January 2023.

[6] Bikash Kunwar, Aashutosh A Mishra, and Imon Chakraborty. Sizing and analysis of canard-wing aircraft with jet propulsion. In *AIAA AVIATION FORUM AND ASCEND 2024*, page 3752, 2024.

[7] John Deyoung. Theoretical symmetric span loading due to flap deflection for wings of arbitrary plan form at subsonic speeds, January 1952. NTRS Author Affiliations: NTRS Report/Patent Number: NACA-TR-1071 NTRS Document ID: 19930092116 NTRS Research Center: Legacy CDMS (CDMS).

[8] RD Finck. Usaf (united states air force) stability and control datcom (data compendium). Technical report, MCDONNELL AIRCRAFT CO ST LOUIS MO, 1978.

[9] Jinggen Zhao. *Dynamic Wake Distortion Model for Helicopter Maneuvering Flight*. PhD thesis, Georgia Institute of Technology, Atlanta, GA, USA, March 2005.

[10] Advanced Precision Composites Propellers. Apc propeller performance data. Online: `https://www.apcprop.com/technical-information/performance-data/`, 2024.

[11] Rajan Bhandari, Aashutosh Aman Mishra, and Imon Chakraborty. Optimization of Lift-Plus-Cruise Vertical Take-Off and Landing Aircraft with Electrified Propulsion. *Journal of Aircraft*, 61(2):392–414, March 2024.

[12] Imon Chakraborty and Aashutosh Aman Mishra. Sizing and analysis of a lift-plus-cruise aircraft with electrified propulsion. *Journal of Aircraft*, 60(3):747–765, 2023.

[13] Imon Chakraborty, Aashutosh Aman Mishra, Dennis van Dommelen, and Willem AJ Anemaat. Design and sizing of an electrified lift-plus-cruise ducted fan aircraft. *Journal of Aircraft*, 60(3):817–834, 2023.

[14] M. Tischler, T. Berger, C. Ivler, M. Mansur, K. Cheung, and J. Soong. *Practical Methods for Aircraft and Rotorcraft Flight Control Design - An Optimization-Based Approach*. American Institute of Aeronautics and Astronautics, 1st edition, 2017.

[15] A Halder, V Agarwal, R Garhwal, and Dr M Sinha. Determination of Inertial Characteristics of a High Wing Unmanned Air Vehicle. April 2008.

[16] William Gracey. The experimental determination of the moments of inertia of airplanes by a simplified compound-pendulum method. Technical report, 1948.

[17] Hartley A Soule and Marvel P Miller. The experimental determination of the moments of inertia of airplanes. Technical report, 1934.

[18] Bikash Kunwar and Imon Chakraborty. Developing Flight Simulation Model for a Lift-Plus-Cruise Subscale Vehicle: Mass Properties, Propulsion, and System Identification. In *AIAA SCITECH 2025 Forum*. American Institute of Aeronautics and Astronautics. _eprint: https://arc.aiaa.org/doi/pdf/10.2514/6.2025-0739.